JMEPEG (2012) 21:1352–1362
DOI: 10.1007/s11665-011-9991-3

1059-9495/$19.00

Removal of Double Oxide Film Defects by Ceramic Foam Filters

Arash Ardekhani and Ramin Raiszadeh

(Submitted September 24, 2010; in revised form April 18, 2011)

In this study, Weibull statistical and statistical image analyses of porosity were employed to determine the efficiency of ceramic foam filters for the removal of double oxide film (bifilm) defects from a pure Al melt. Using these efficiencies and the branch filter model, the average size of the inclusions present in the liquid was estimated, and assuming that most of the inclusions in the melt are in the form of double oxide films, the possible dimensions for these defects were calculated. The results showed that the foam filters can remove oxide defects from the melt and that the efficiency of this filtration depends on the pore size of the filter. The average dimension of the oxide film defects was calculated to be 13.8 × 13.8 μm with a maximum thickness of 1 μm, if they remained non-convoluted in the metal flow. If they became convoluted because of the turbulence of the liquid flow, then the dimensions of the flat defect before it became curled up in the flow were calculated to be between 37 × 37 × 1 and 370 × 370 × 0.01 μm.

Keywords bifilm, double oxide film defect, foam filter, melt quality

1. Introduction

Aluminium alloy castings are increasingly commonplace in applications, such as the automotive and aerospace industries, where their mechanical properties must be reliable and reproducible. A common casting defect with a random nature that significantly reduces the reliability of Al (and Mg) alloy castings is the double oxide film defect, the formation of which was discussed by Campbell (Ref 1). During the casting process, the surface of the liquid metal can fold over upon itself, and the opposing surface oxide films come into contact with each other, trapping a volume of gas (presumably predominantly air). This forms a discontinuity or crack in the matrix of the solidified casting that not only reduces the mechanical properties of the casting, but can also act as an initiation site for the formation of other defects, such as hydrogen pores (Ref 2, 3) and Fe-rich phases (Ref 4).

The initial dimensions of a newly formed double oxide film defect in Al castings are not known. However, Campbell (Ref 1) suggested their dimensions to be of a few millimetres in length and width and a thickness on the order of nanometers. It has been proposed (Ref 1) that once the doubled oxide film defects become entrained in the melt, they can become convoluted because of turbulence in the bulk liquid as the liquid metal fills the mould. However, it was proposed that the oxide film defects could be expanded again because of a variety of effects, such as the precipitation of dissolved hydrogen from the surrounding melt into the internal atmosphere trapped within them, and strains in the liquid metal due to solidification shrinkage (Ref 1, 5-7).

The use of ceramic foam filters in the casting of metals for the removal of inclusions from the melt has become ever more common where the quality of the cast product is a dominant issue. The action of a ceramic foam filter to stop double oxide films in Al alloys has, in general, not been clearly recognized (Ref 8). This, according to Campbell, is probably because the films are so thin that they cannot be detected when wrapped around sections of the ceramic filter.

Din et al. (Ref 9), who studied the effect of using ceramic foam filters in a direct pour system on the tensile properties of A356 Al alloy, showed that only about 10% of the benefit of using a filter in the running system is derived from the prevention of solid inclusions from entering the mould cavity and that the other 90% is actually from the improvement in the filling behavior of the casting. The velocity of the flow decreases in the running system as it passes through a filter. A filter also reduces the time for back-filling of the sprue and smoothes fluctuations in the flow. All these effects reduce the formation of double oxide film defects in the running system during filling (Ref 10) and, therefore, improve the quality and the reliability of the casting. The effect of a ceramic filter on the reduction of flow velocity has not so far been studied extensively. However, Habibollahzadeh and Campbell (Ref 11) measured about a 75-80% reduction in flow velocity in both Al-Si and cast iron alloys as they passed through a 20 ppi (pores per linear inch) foam filter. Hashemi and Raiszadeh (Ref 12) reported this reduction in Al-Si alloy to be about 50%.

Three general mechanisms for the filtration of solid particles from liquid have been recognized (Ref 13), namely, sieving of coarse particles that are physically unable to pass through the

Arash Ardekhani and **Ramin Raiszadeh**, Department of Metallurgy and Materials Science, Shahid Bahonar University of Kerman, Jomhoori Eslami Blvd., Kerman, Iran; and **Arash Ardekhani** and **Ramin Raiszadeh**, Mineral Industries Research Centre, Shahid Bahonar University of Kerman, Jomhoori Eslami Blvd., Kerman, Iran. Contact e-mails: arash_5015801@yahoo.com and rraiszadeh@yahoo.com.

filter cells, cake filtration of fine particles being physically trapped by a cake layer on the inlet face of filters, and deep bed filtration of fine inclusions, which are attracted physicochemically to the filter media wall by surface energy forces and then sintered to the filter material. Woven cloth filters mainly operate in the first two modes, and the third mode usually occurs within granular or foamed filter media (Ref 14). More than one mode of filtration is usually present in most filtration processes (Ref 13).

The filtration mode by which double oxide film defects might be removed from the melt is not known. However, it should depend on the morphology of the defect (i.e., convoluted or opened-up). Sieving or cake filtration seems to be the main filtration mechanism if the oxide defects are not convoluted (Ref 8). In a convoluted form, depending on the diameter of the defects (which is also not known), any of the three modes might be effective during filtration. To date, this matter has not been studied.

Several mathematical models have been developed to study the transport and capture of particles in porous media. These models are summarized in the literature (Ref 15). The aim of many of these models is to estimate the filtration efficiency E, which follows an exponential law and is expressed as follows (Ref 16, 17) (all the parameters are defined in Table 1):

$$E = 1 - \frac{C_{\text{out}}}{C_{\text{in}}} = 1 - \exp(-\eta a_s b H) \quad \text{(Eq 1)}$$

Assuming that the main mechanisms by which solid particles are captured in a foam filter is interception, Ciftja et al. (Ref 16) adopted three filter models from the literature, namely, isolated sphere with potential flow (IS-PF) (Ref 17), isolated sphere with creeping flow (IS-CF) (Ref 18), and the constricted-tube model (Ref 18) to derive expressions for the filtration efficiency (see Eq 2-4). The details of these models can be found in the literature. In all of these models, it is assumed that all of the forces acting on a particle in a fluid stream are negligible and that the particle will move along with the streamlines. It is also assumed that any particle that comes within one particle radius from the wall will be deposited in the filter and, therefore, removed from the melt.

Table 1 Nomenclature

C_{in}	Number of inclusions per unit volume that enters the filter
C_{out}	Number of inclusions per unit volume that exit the filter
η	Collision efficiency (number of particles removed/number of particles approaching the collector)
a_s	Surface area of collector per unit volume of melt, m^2
b	Ratio of the collector surface area projected in the direction of flow to the total collector surface area
H	Filter thickness, m
a	Inclusion radius, m
R	Filter cell radius, m
ε	Filter porosity (void fraction)
E	Filtration efficiency
N_R	$= a/R$
d_g	$= 2R$, m
d_c^*	Dimensionless constriction diameter defined as d_c/d_g
d_c	Constriction diameter, m
ℓ	Mean pore height, m
R_b	Branch radius, m

$$E_{\text{Sphere}}^{\text{pot.flow}} = 1 - \exp\left[-\frac{9a(1-\varepsilon)}{4R^2\varepsilon}H\right] \quad \text{(Eq 2)}$$

$$E_{\text{Sphere}}^{\text{creep.flow}} = 1 - \exp\left[-\frac{9N_R^2(1-\varepsilon)}{8R\varepsilon}H\right] \quad \text{(Eq 3)}$$

$$E_{\text{const-tube}} = 1 - \exp\left(\frac{3}{2}\left(\frac{4N_R^2}{d_c^{*2}} - \frac{4N_R^2}{d_c^{*3}} - \frac{N_R^4}{d_c^{*4}}\right) \times \frac{\left(d_g^2 - d_c^2\right)(1-\varepsilon)}{\left(\frac{d_c^2}{2} + d_g^2\right)\ell\varepsilon} H\right) \quad \text{(Eq 4)}$$

In these three models, the particle collectors are considered to be spheres and tubes. According to Ciftja et al. (Ref 16), ceramic foam filters do not comprise spheres, tubes, or empty pores but comprise many small branches that form a network. Ciftja et al. considered these branches, which collect the particles, to be cylinders having a radius of one-tenth of that of the spheres in the previous three models, and derived a new expression for the filtration efficiency, named the branch model (Eq 5).

$$E_b = 1 - \exp\left[-\frac{4a(1-\varepsilon)}{\pi R_b^2 \varepsilon}H\right] \quad \text{(Eq 5)}$$

When comparing the filtration efficiencies obtained experimentally during the filtration of SiC and Si_3N_4 inclusions from molten silicon with a 30 ppi ceramic filter to those calculated by the four models, Ciftja et al. concluded that the branch model was the most accurate one.

In this study, Weibull statistical and statistical image analyses of porosity were employed to determine the efficiency of ceramic foam filters with pore sizes of 10, 20, and 30 ppi for the removal of double oxide film defects from pure Al melt. Afterward, the average defect size was estimated using the four filter models described above. The effect of designing a bad running system on the reduction of filtration efficiency has also been demonstrated.

2. Experimental Procedure

A cylinder 180 mm in diameter and 200 mm in height was cast using a naturally-pressurized running system with a pouring rate of 1 kg s^{-1} (see Fig. 1). The running system had been designed to cause splashing of the liquid metal in the sprue and, hence, entrainment of the oxidized surface of the melt in it and to maintain the melt in the rest of the system (i.e., runner and gate) surface-turbulence free. The running system dimensions, shown in Table 2, were chosen to ensure that the melt entered the mould cavity with a velocity less than 0.5 m s^{-1}. Therefore, no oxide film defects were formed in the running system, except in the sprue. The actual ingate velocity was measured experimentally (by capturing the liquid metal flowing out of a gate on video tape) to be about 0.4 m s^{-1}.

Four experiments were carried out, one without using a filter and three with 10, 20, or 30 ppi alumina ceramic foam filters inserted in the runners. The orientation of the filter was adopted

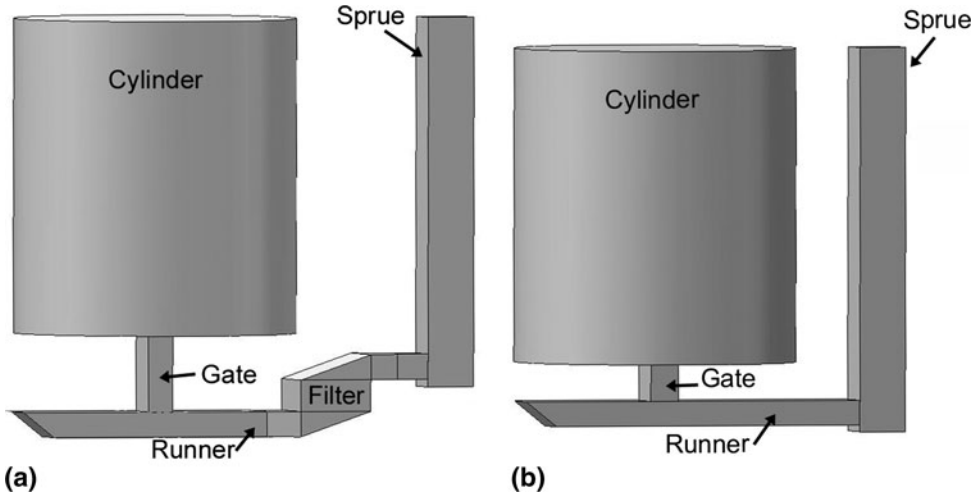

Fig. 1 Schematic sketch of the moulds used in this research: (a) the mould with a filter inserted in its runner, and (b) the mould without a filter. The dimensions are shown in Table 2

Table 2 Dimensions of the running system components shown in Fig. 1 (all in mm)

Component	Cylinder mould without filter	Cylinder mould with filter
Sprue	30 × 30 × 245(a)	30 × 30 × 235
Filter	…	20.9 × 46 × 48
Runner	16 × 30 × 200	16 × 30 × 160
Gate	16 × 30 × 25	16 × 30 × 50
Cylinder	ϕ = 180, *h* = 200	ϕ = 180, *h* = 200

(a) The first two figures are the cross section dimensions

from Ref 8. Each experiment was repeated three times to ensure the repeatability of the results. The moulds were prepared using silica sand (AFS grain size of 73), 5% sodium silicate and CO_2 gas. 20 kg of commercial purity Al alloy (>99.7 wt.% Al) was melted in an electric furnace and poured into the moulds with a temperature of 750 °C. 25 tensile test samples and 10 metallography specimens were cut out of each cylinder, as shown in Fig. 2.

The test bars were machined to the dimensions shown in Fig. 2 and tested using a Zwick 1484 tensile testing machine with a strain rate of 1 mm min^{-1}. The fracture surfaces of the failed test bars were examined using a Camscan Scanning Electron Microscope fitted with an Oxford Inca EDX for microanalysis, employed to confirm the presence of oxide film defects on the fracture surfaces. The UTS values obtained were analyzed using a two-parameter Weibull distribution to assess the scatter of the mechanical properties (Ref 19). The Weibull modulus (the slope of the line fitted to the Weibull cumulative distribution data) is a single value that describes the spread of properties. A higher Weibull modulus is indicative of a narrower spread of properties, and in this case, is an indication of a casting that has a lower amount of defects and greater reproducibility of properties.

The ten metallography samples were examined by optical microscopy after being polished to 1 μm. Porosity parameters, namely, the pore number density (i.e., number of pores per unit area of the examined cross section), %porosity content (per cent of the cross section occupied by pores), and mean pore roundness (see Eq 6 for its definition), were estimated using Pixcavator IA 4.3 image analysis software on optical microscopy images taken with a magnification of ×50 on all the metallography samples. The efficiency of the filter was also calculated using Eq 1, in which C_{out} and C_{in} were considered to be the pore number densities measured in the cylinders that were cast with and without a filter, respectively.

$$\text{Pore roundness} = \frac{4\pi(\text{pore area})}{(\text{pore perimeter})^2} \times 100 \qquad \text{(Eq 6)}$$

The metallography samples were also examined by SEM and EDX to detect any oxide films or other inclusions, which were associated with the pores formed in them.

To observe the flow behavior of the liquid metal through the filter, in some experiments, a piece of heat-resistant glass was inserted at the location of the filter in the wall of the sand mould, and the flow of the liquid metal was captured on video tape using a Sony video camera with a 30 fps shutter speed. The video was then converted to JPEG pictures using Adobe Premiere 2 Software.

In a recent study, Hashemi and Raiszadeh (Ref 12) showed that if the height of the runner after the filter was higher than the critical height (i.e., the maximum height from which a liquid metal can fall without reaching critical velocity, about 12 mm for Al alloys; Ref 8), considerable amounts of double oxide film defects were formed after the filter. To investigate this matter, the experiments with 10 and 30 ppi filters described above were repeated with the height of the runner doubled (from 16 to 32 mm).

To provide an idea about the possible dimensions of the oxide film defects, the filtration efficiency obtained for each filter size was put in the filter model (this method was repeated for each filter model presented in Eq 2-5), and the particle diameter corresponding to this efficiency was calculated. The parameters used in these calculations are presented in Table 3. The average of the particle diameters obtained in this way for the three filter sizes was assumed to be the best estimate for the average diameter of the inclusions that were present in the melt. The filtration efficiency for each filter size was then calculated using this average inclusion diameter and the relative standard error of

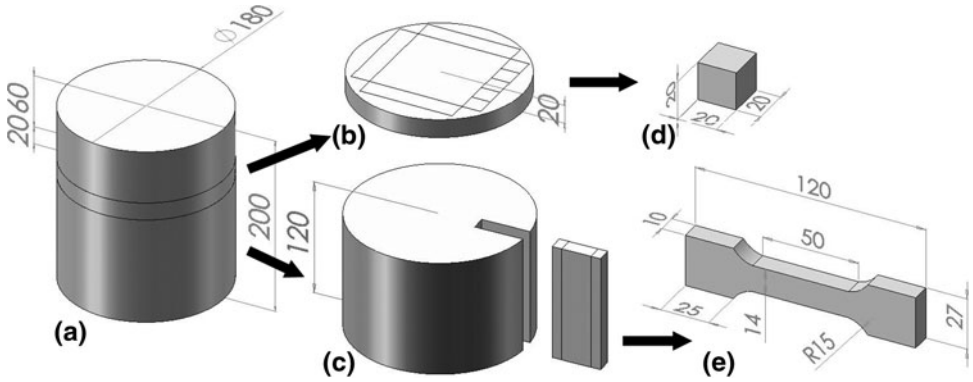

Fig. 2 Sketch of the machining method used to obtain the tensile test and metallography samples. The solidified ingot obtained from each experiment (a) was first cut into 20- and 120-mm thick slices (b and c, respectively), and then into 10 metallography and 25 tensile test samples (d and e, respectively)

Table 3 Parameters used in calculations for estimations of the average defect size

Parameter	Value		
	10 ppi	20 ppi	30 ppi
H, filter thickness, mm	20.9	20.9	20.9
ε, filter void fraction(a)	0.693	0.714	0.734
R, collector radius, mm	2.4 (Ref 23)	1.65 (Ref 23)	0.983 (Ref 24)
d_c, filter window diameter, mm	1.778 (Ref 25)	1.222 (Ref 25)	0.728 (Ref 24, 26)
ℓ, mean pore height, mm(b)	4.8	3.3	1.965
R_b, branch radius (1/10 of R; Ref 16), mm	0.24	0.165	0.0983

(a) Measured using Archimedes displacement method. (b) Assumed to be equal to the filter cell diameter

these efficiencies compared to those obtained experimentally was calculated. By this method, the average diameter of the inclusions presented in the melt, and the relative standard error (which indicates the closeness of the estimated values to those obtained experimentally) were estimated for each filter model.

According to Campbell (Ref 1), all the exogenous inclusions in the liquid aluminium are in the form of double oxide defects. Adopting this theory, the particle diameters estimated from the filter models were attributed to the dimensions of double oxide film defects presented in the liquid metal.

3. Results

3.1 The Results Obtained from the Tensile Test Bars

Figure 3 shows the Weibull plots for UTS values obtained from each experiment (with a runner of 16 mm in height). A summary of these has also been shown in Table 4. These results show that using a ceramic filter in the runner increased the Weibull modulus considerably, an indication of fewer defects present in the castings. The results also show that the Weibull modulus increased as the pore size of the ceramic filter decreased (i.e., ppi, pores per linear inch of the filter, increased), from 12.07 for the test bars that were cast without using a filter to 19.01, 24.17, and 28.33 for the test bars that were cast using 10, 20 and 30 ppi filters, respectively.

However, the ceramic filter did not have such a significant effect on the Weibull modulus when the height of the runner was increased from 16 to 32 mm. Figure 4 shows the Weibull

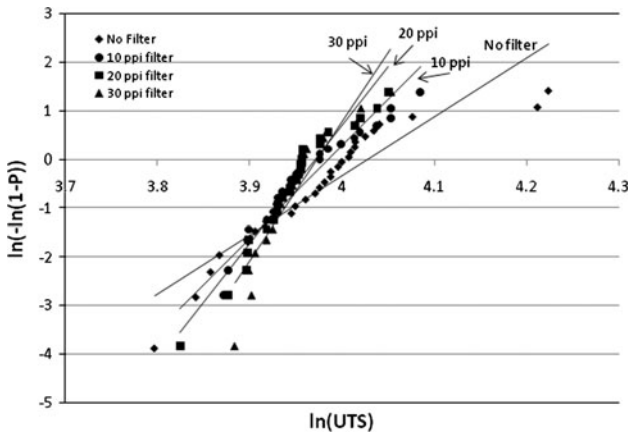

Fig. 3 Weibull plots for the UTS values obtained from the tensile test bars that were cast without a filter and with 10, 20, and 30 ppi filters, and a 16-mm high runner

plots for the UTS values obtained from the tensile test bars that were cast with a 32-mm high runner. The Weibull moduli and the scale parameters obtained for these experiments are also shown in Table 4. It is seen that with a runner 32 mm in height, the Weibull modulus of 12.07 (for the test bars cast without a filter) increased slightly to 13.81, and then further to 18.33, for those that were cast using a 10 and 30 ppi ceramic filters, respectively.

SEM and EDX studies revealed the presence of a high number of oxide films on the fracture surfaces of the test bars

Table 4 Summary of Weibull moduli and scale parameters for UTS values

Runner height, mm	Experiment	Number of samples	Weibull modulus	Scale parameter	Regression coefficient
16	No filter	25	12.07	55.08	0.858
16	10 ppi	25	19.01	53.77	0.928
16	20 ppi	25	24.17	54.05	0.935
16	30 ppi	25	28.33	53.12	0.864
32	10 ppi	24	13.81	52.24	0.984
32	30 ppi	25	18.33	53.67	0.983

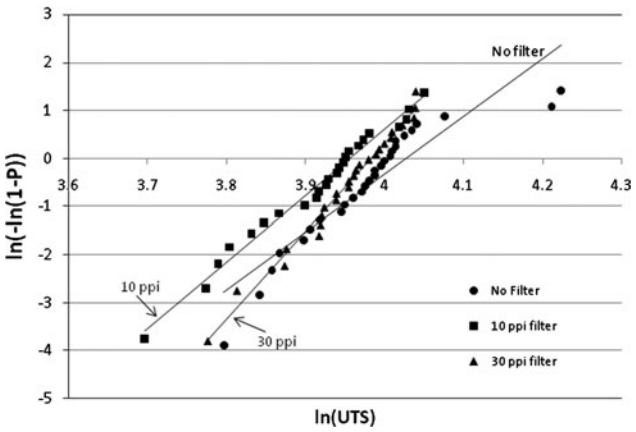

Fig. 4 Weibull plots for the UTS values obtained from the tensile test bars that were cast without a filter and with 10, 20, and 30 ppi filters, and a 32-mm high runner

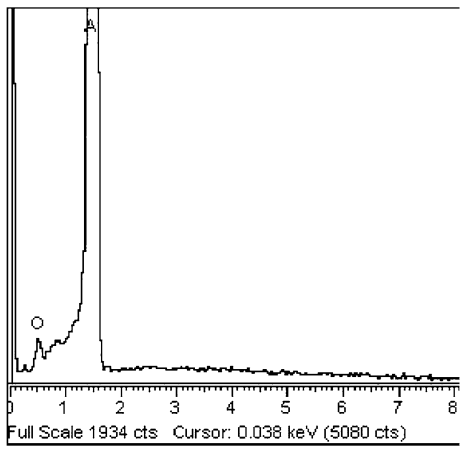

Fig. 6 EDX spectrum obtained from point P1 given in Fig. 5. The concentration of O at this point was measured to be 2.95 wt.%

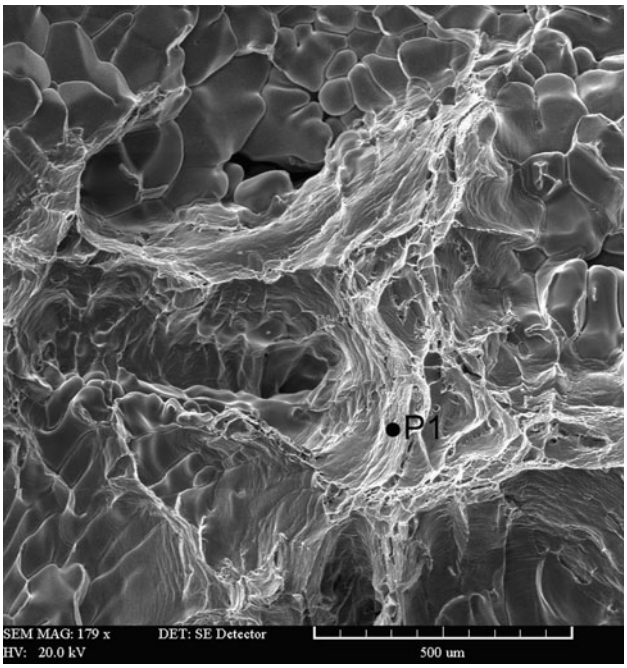

Fig. 5 SEM micrograph from the fracture surface of a tensile test bar cast without a ceramic filter, showing an oxide layer spread on the microstructure. The EDX spectrum obtained from point P1 is shown in Fig. 6

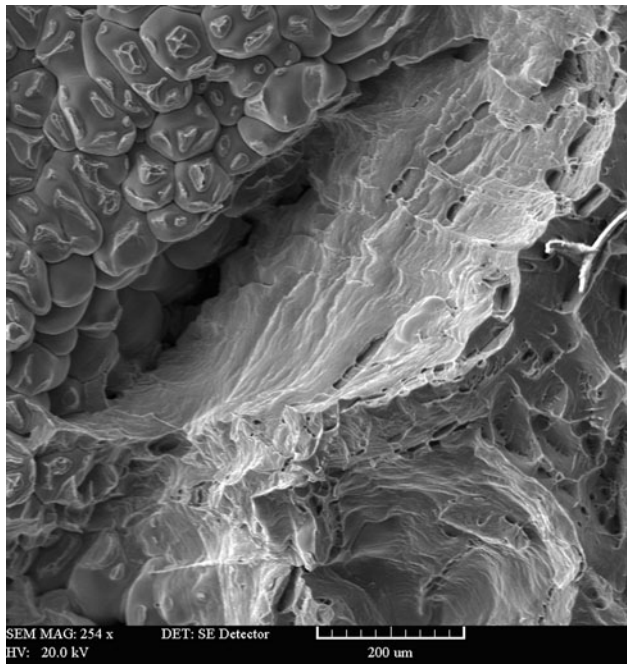

Fig. 7 SEM micrograph obtained from the fracture surface of a tensile test bar cast without a ceramic filter, showing an oxide layer adjacent to a pore, and small oxide film fragments scattered on the surface of the Al dendrites in the pore

that were cast without using a filter (see Fig. 5, 6), many of them associated with pores. Figure 7 shows an oxide layer adjacent to a pore formed in the fracture surface of a test bar, and small oxide film fragments (the identity of which was confirmed by EDX) scattered on the surface of the Al dendrites in the pore.

The fracture surfaces of the test bars cast using a 10 ppi ceramic filter (and a 16-mm high runner) were also decorated with networks of oxide films and small oxide fragments on the surface of the Al dendrites inside the pores. The number of oxide films was less than those for test bars cast without a filter. Figure 8 shows an example of an oxide film network associated with a pore. The identity of the feature labeled P1 was confirmed by EDX analysis (shown in Fig. 9).

The number of oxide films observed on the fracture surfaces of the test bars cast with a 20 ppi ceramic filter and a runner height of 16 mm was considerably less than those cast without a filter or with a 10 ppi filter. However, networks of oxide films associated with pores could occasionally be observed on the fracture surfaces. Figure 10 shows an example of an oxide film network (indicated by an arrow) associated with a pore that formed on the fracture surface of a test bar that was cast with a 20 ppi filter.

No oxide film was observed in the microstructure of the test bars that were cast using a 30 ppi ceramic filter and a runner height of 16 mm (see Fig. 11). The fracture surfaces of these bars showed features associated with ductile failure. This implies that the fracture mechanism in these test bars was different from those described above.

The SEM micrographs taken from the fracture surfaces of the test bars that were cast with 10 ppi or 30 ppi filters and a

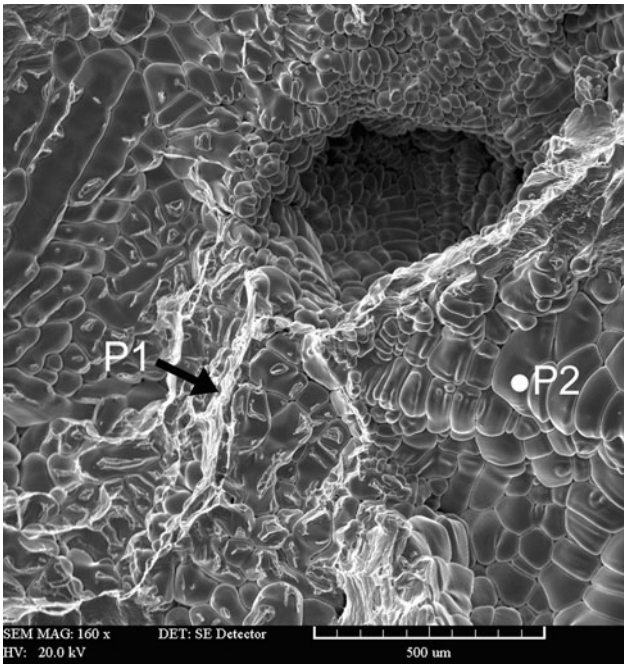

Fig. 8 SEM micrograph obtained from the fracture surface of a tensile test bar cast using a 10 ppi ceramic filter and a 16-mm high runner, showing an oxide film network (denoted P1) associated with a pore. The EDX spectra obtained from point P1 and P2 are shown in Fig. 9

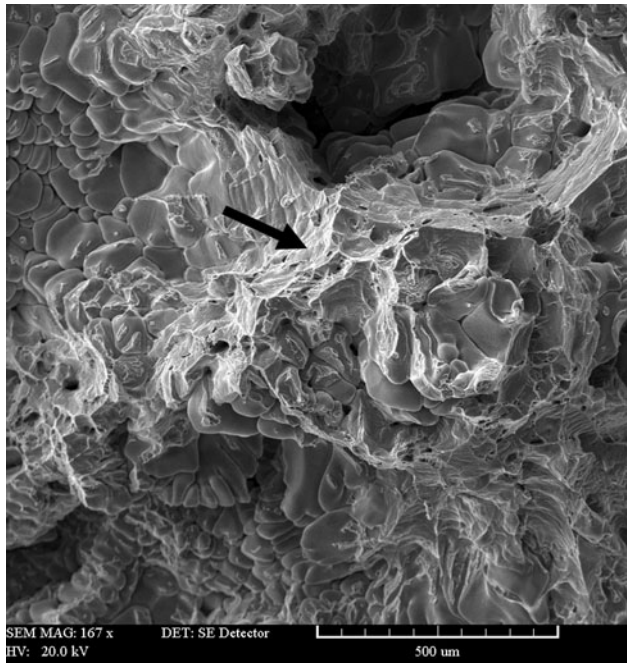

Fig. 10 SEM micrograph obtained from the fracture surface of a tensile test bar cast using a 20 ppi ceramic filter and a 16-mm high runner, showing an oxide film network (indicated by arrow) associated with a pore

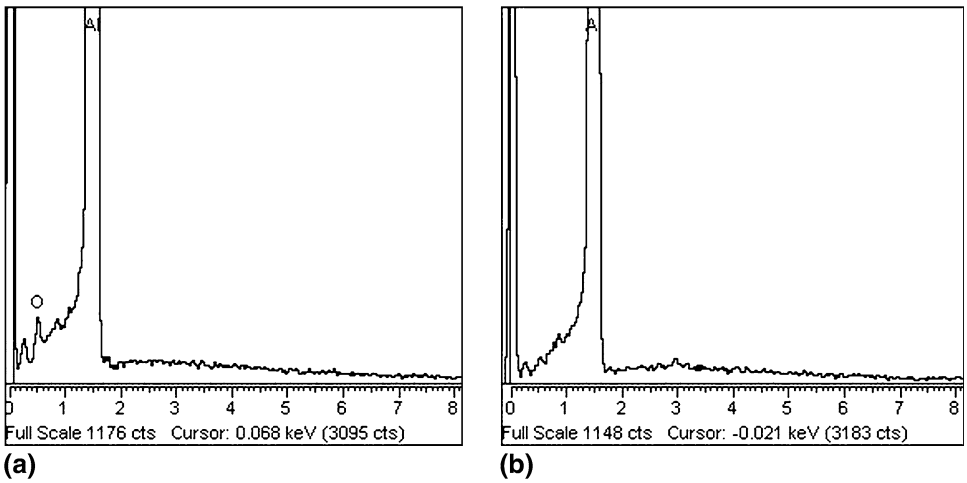

Fig. 9 EDX spectra obtained from (a) point P1 and (b) point P2 given in Fig. 8. The concentration of O was measured to be 3.52 wt.% at point P1 and 0 wt.% at point P2

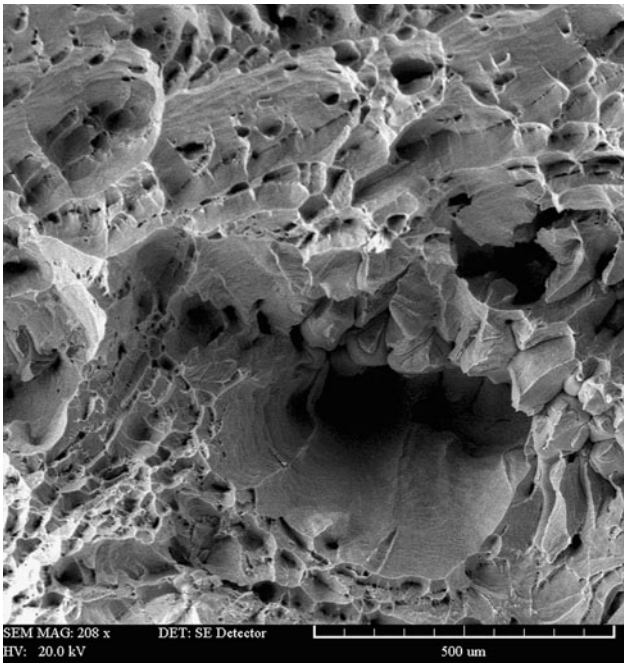

Fig. 11 SEM micrograph obtained from the fracture surface of a tensile test bar cast using a 30 ppi ceramic filter and a 16-mm high runner. No oxide film was observed in the microstructure

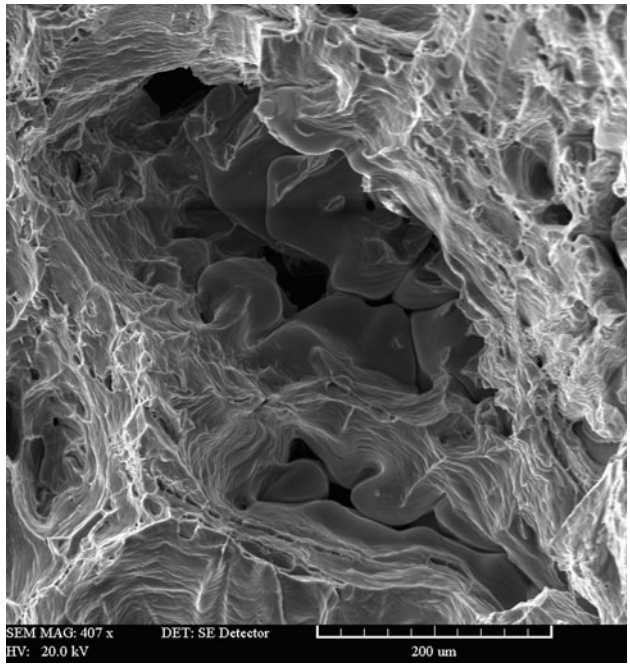

Fig. 12 SEM micrograph obtained from the fracture surface of a tensile test bar cast using a 30 ppi ceramic filter and a 32-mm high runner, showing an oxide film network around a pore, and oxide fragments on the dendrites inside the pore

Table 5 Porosity parameters measured on the metallography specimens

Runner height, mm	Experiment	Pore number density, mm^{-2}	Porosity, %	Mean roundness	Mean pore area, mm^2	Filtration efficiency, %	Weibull modulus
16	No filter	0.294	33.3	26.82	0.012	0	12.07
16	10 ppi	0.080	11.9	25.55	0.003	72.6	19.01
16	20 ppi	0.015	0.93	21.55	0.005	94.8	24.17
16	30 ppi	0.0004	0.02	28.77	0.008	99.9	28.33
32	10 ppi	0.100	13.6	20.73	0.016	65.7	13.81
32	30 ppi	0.068	4.3	23.61	0.039	76.9	18.33

32-mm high runner showed numerous networks of oxide films, many of them associated with pores, and oxide fragments on the dendrites inside the pores. An example from the fracture surface of a test bar cast using a 30 ppi filter is presented in Fig. 12.

3.2 The Results Obtained from the Metallography Samples

The porosity parameters calculated from the image analysis results of the optical micrographs taken from the cross sections of the tensile test bars that were cast with a 16- or 32-mm high runner and different filters, along with the Weibull moduli, are summarized in Table 5. It is seen that the pore number density and %porosity were the only porosity parameters that had a correlation with the pore size of the ceramic filter and the filtration efficiency, both following the same trend. The pore number densities as well as the filtration efficiencies are shown graphically in Fig. 13.

Figure 13 shows that using a 10 ppi ceramic filter in the runner caused the pore number density in both of the cylinders that were cast using 16- and 32-mm high runners to decrease (by about 72 and 66%, respectively) and the filtration efficiency to increase (by about 73 and 68%, respectively). This figure also shows that the porosity parameter decreased and the filtration efficiency increased further as the pore size of the filter decreased.

However, the effects of a ceramic filter on the reduction of pore number density and the increase in the filtration efficiency were much more prominent when a 16-mm high runner was used. The pore number density of the cylinder that was cast using a 30 ppi filter and a 16-mm high runner was measured to be almost zero, and its filtration efficiency was almost 100%, whereas the pore number density and the filtration efficiency of the cylinder that was cast with a 30 ppi filter and a 32-mm high runner were measured to be about 0.068 mm^{-2} and 76.9%, respectively.

The cause of the difference in the efficiencies of the filters when used in 16- and 32-mm high runners is revealed by the pictures taken from the liquid when it was flowing through the filter (for example, see the pictures shown in Fig. 14, which were taken of the liquid metal when it was passing through a 10 ppi filter inserted in a 32-mm high runner). It is evident that the liquid metal first accumulated on the top face of the ceramic filter and could not pass through it (see Fig. 14a, b).

Subsequently, the metal passed through the filter as several separate streams (Fig. 14c), each of which was covered by an Al_2O_3 tube.

According to Campbell (Ref 1), if the height of these falling streams is greater than the critical height of 12.5 (in Al alloys), then the shear force of the falling liquid is great enough to tear the oxide layer around the stream and entrain it continuously into the bulk liquid. The pictures obtained from video recordings revealed that the falling height of the liquid stream in the 32-mm high runner decreased to below this critical height in 1.13, 3.5 and 4 s, when filled through a 10, 20 or 30 ppi filter, respectively. These times decreased significantly to 0.2, 0.6 and 0.7 s, respectively, in the 16-mm high runner. The almost 100% efficiency of the 30 ppi filter implied that the fall of the liquid metal into the 16-mm high runner during such short times did not produce a significant amount of oxide film defects.

With a few exceptions, the SEM micrographs and EDX spectra obtained from the metallography specimens taken from the cylinders that were cast using 10, 20, and 30 ppi ceramic filters showed no evidence of inclusions in the pores other than the oxide film layers at the inner surfaces of the pores (see for example Fig. 15, 16).

Figure 17 shows the relationship between the filtration efficiencies and the Weibull moduli obtained from the experiments. It can be seen that using a ceramic filter with an efficiency of less than 65% (i.e., a coarse filter of 10 ppi in a poorly designed runner that is 32 mm in height) did not cause the Weibull moduli of the test bars to increase significantly. This figure also shows an almost linear relationship between the Weibull modulus and the filtration efficiency when the filtration efficiency is greater than 65%.

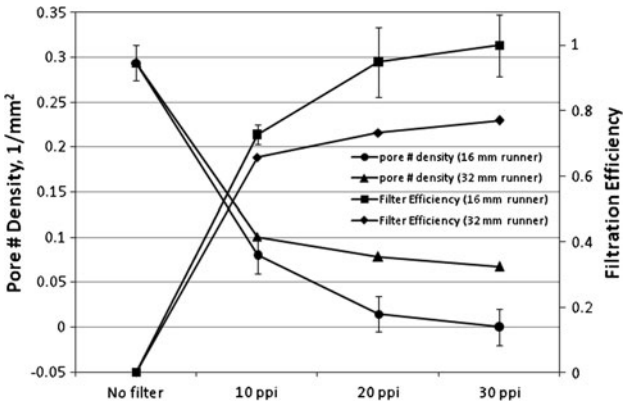

Fig. 13 The pore number density and filtration efficiency calculated from the image analysis results of the optical micrographs

3.3 The Estimation of the Average Size of the Defects

The diameters of the double oxide film defects that were calculated by the four filter models for each filter pore size are presented in Table 6. It can be seen that the diameters calculated by the four models differ significantly from each other. The largest average radius (2240 μm) was calculated by the IS-CF model, whereas the smallest average radius (13.8 μm) was calculated by the branch model. The average diameters calculated by the other two models were between these two values, 776 and 430 μm, and calculated by the IS-PF and constricted-tube modes, respectively.

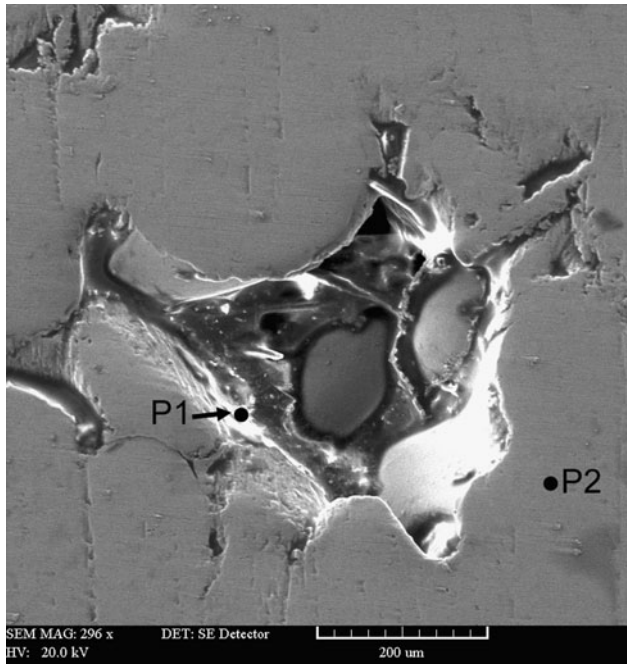

Fig. 15 SEM micrograph obtained from a metallography specimen taken from the cylinder cast using a 20 ppi filter, showing an oxide layer that covers the internal surface of the pore. The EDX spectra obtained from points P1 and P2 are shown in Fig. 16

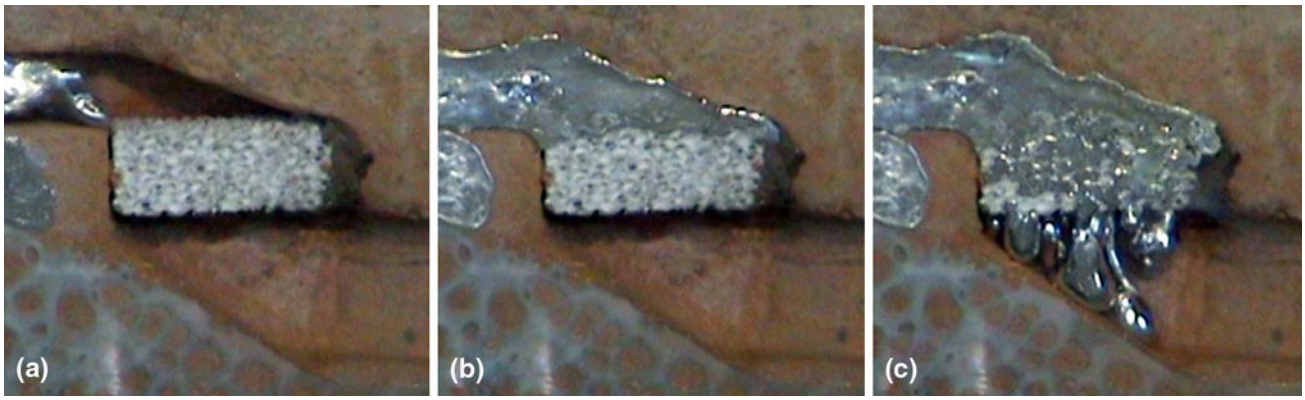

Fig. 14 An example of the pictures taken from the liquid metal when it was passing through a 10 ppi ceramic filter inserted in a 32-mm high runner. The metal first got accumulated on the top face of the filter (a, b) and then passed through the filter as several separate streams (c)

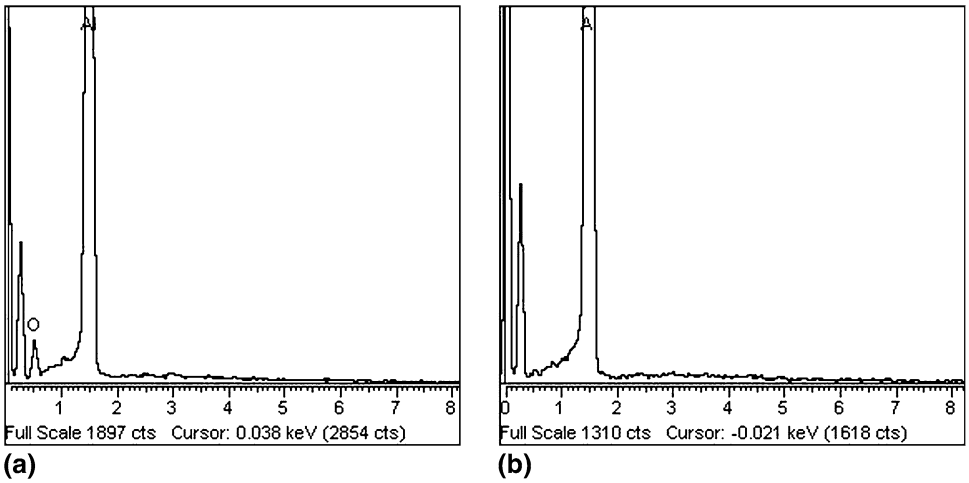

Fig. 16 EDX spectra obtained from (a) point P1 and (b) point P2 given in Fig. 15. The concentration of oxygen was measured to be 5.4 and 0 wt.% at points P1 and P2, respectively

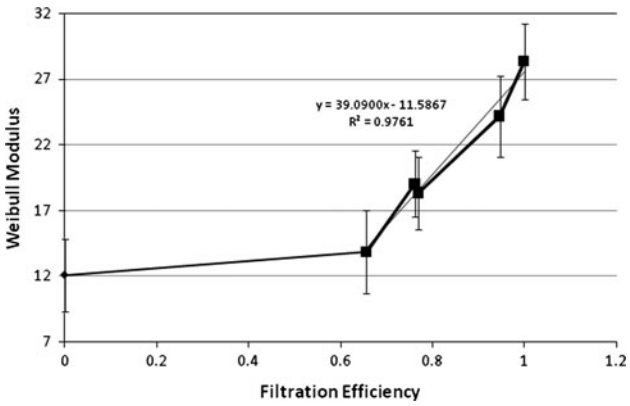

Fig. 17 Relationship between the filtration efficiency and the Weibull modulus

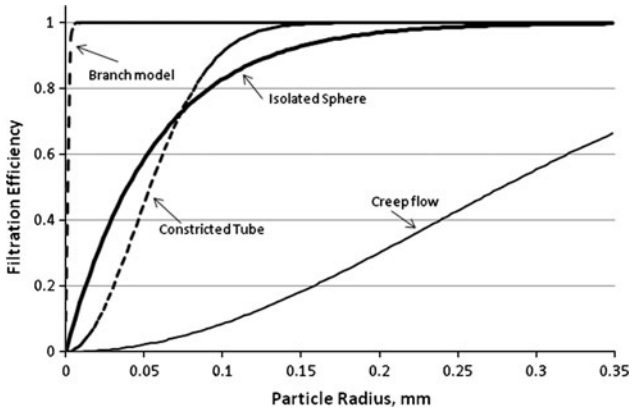

Fig. 18 Filtration efficiencies of a 30 ppi ceramic filter, calculated using the four filter models (Eq 2-5)

Table 6 Average double oxide film defect diameter, in µm, calculated using Eq 2-5

From the efficiency obtained for	Isolated sphere potential flow	Isolated sphere creep flow	Constricted-tube model	Branch model
10 ppi filter	716	2624	504	12.6
20 ppi filter	856	2374	456	15.2
30 ppi filter	754	1722	328	13.4
Average	776	2240	430	13.8
Relative standard error, %	9.3	20.8	21.2	9.3

The relative standard error obtained for each filter model, also presented in Table 6, indicates how close the filtration efficiencies calculated by the filter model were to the experimentally measured ones. It can be seen that the average radius sizes calculated by the IS-PF and branch models has the least relative standard errors (9.3%) among the four models.

4. Discussion

The results obtained in this research clearly show that the ceramic foam filters commonly used in foundry industries can remove double oxide film defects from liquid aluminum and that the efficiency of this filtration depends on the pore size of the filter. The smaller the pore size of the filter, the higher the efficiency of the filtration, so that a 30 ppi ceramic filter could eliminate almost all of the oxide film defects from a casting.

The filtration efficiencies calculated by the four filter models (Eq 2-5) for a particle with a known dimension, are significantly different from each other (see Fig. 18). For example, for a 50-µm diameter particle, the filtration efficiency of a 30 ppi ceramic filter is calculated to be 34, 0.5, 13, and 100% by IS-PF, IS-CF, constricted-tube, and branch models, respectively. However, the relative standard errors shown in Table 6 revealed that the IS-PF and branch models were more compatible than

the other two models with the experimental results obtained in this study.

The expressions of the IS-PF and branch models have the same general shape, and hence, their relative standard errors being equal could be expected. The main difference between the two models is in the filter collector diameter. While the collector diameter in the branch model is 1/10 of that in the IS-PF model (Ref 16), the filter efficiency calculated by the branch model for a particular particle size is much higher than that of the IS-PF model. Comparing the experimental results with the results obtained from the four models, Ciftja et al. (Ref 16) concluded the branch model to be the most accurate. Although this claim could not be verified in this research, based on the Ciftja et al. experimental results and also the relative standard errors obtained in this research, the branch model was chosen as the best model for calculating the efficiency of the foam filters.

Using Stokes law (Ref 20), Raiszadeh (Ref 6, 21) predicted that the thickness of a flat oxide film defect suspended in a liquid Al melt could not be greater than 1 μm, as otherwise its buoyancy causes the defect to float out of the metal (or attach to the upper surface of the gating system) in a short time. Campbell (Ref 1) speculated this thickness to be only a few nanometers.

The average oxide film diameter was calculated by the branch model to be 13.8 μm. However, it is not known whether the defect was convoluted or not when it passed through the pores of the filter. If non-convoluted, then the defect is assumed to be in the shape of a rectangular cube, with its largest dimensions to be 13.8 μm (e.g., 13.8×13.8 μm with a maximum thickness of 1 μm). If the oxide defect, as was suggested by Campbell (Ref 1), became convoluted to a spherical shape because of the turbulence of the liquid flow, then the dimensions of the defect before it became curled up in the metal flow could be estimated to be of any size between $37 \times 37 \times 1$ to $370 \times 370 \times 0.01$ μm.

Commercial purity Al alloy has a very short freezing range (650-655 °C; Ref 22), and its solidification normally comprises concentrated shrinkage voids, but not porosity. The oxide layers that covered the internal surfaces of the pores (Fig. 15), and the small oxide film fragments scattered on the surface of the dendrites inside the pores (Fig. 7, 8, 10) revealed that the porosity in the cylinders formed, as Raiszadeh and Griffiths suggested recently (Ref 6), because of the diffusion of hydrogen dissolved in the liquid metal into the atmosphere trapped within double oxide film defects, causing the trapped atmosphere to expand and the defects to rupture. Thus, the two porosity parameters, i.e., %porosity and the pore number density could be considered to be two criteria by which the density of the double oxide film defects can be evaluated in castings with a low freezing range.

The experiments with 32-mm high runners clearly showed that if the melt issuing from the filter is allowed to jet into the air, double oxide film defects will be created after the filter and the efficiency of the filter will be diminished. This issue underlines the importance of a proper filter design in the running system if a ceramic filter is to have the maximum efficiency for the removal of double oxide film defects from the melt.

5. Conclusions

(1) Ceramic foam filters can remove double oxide film defects from liquid Al melt. The efficiency of the filtration depends on the pore size of the filter, so that a 30 ppi ceramic filter can eliminate almost all of the oxide film defects from a casting.

(2) If the melt issuing from the filter is allowed to jet into the air, then double oxide film defects will be created after the filter, and the efficiency of the filter will be diminished.

(3) If the filtration efficiency is less than 65%, then the use of the filter does not have any significant effect on the reproducibility of the mechanical properties.

(4) For filtration efficiencies greater than 65%, the Weibull modulus of the casting increased linearly with the filtration efficiency.

(5) The average dimensions of the oxide film defect were calculated by the branch model to be 13.8×13.8 μm with a maximum thickness of 1 μm, if it remains non-convoluted in the metal flow. If it becomes convoluted because of the turbulence of the liquid flow, the dimensions of the flat defect before it became curled up in the flow were calculated to be between $37 \times 37 \times 1$ and $370 \times 370 \times 0.01$ μm.

References

1. J. Campbell, *Castings*, 2nd ed., Butterworth-Heinemann, Oxford, 2003
2. S. Fox and J. Campbell, Visualisation of Oxide Film Defects During Solidification of Aluminum Alloys, *Scripta Mater.*, 2000, **43**, p 881–886
3. W.D. Griffiths and R. Raiszadeh, Hydrogen, Porosity and Oxide Film Defects in Liquid Al, *J. Mater. Sci.*, 2009, **44**, p 3402–3407
4. X. Cao and J. Campbell, The Nucleation of Fe-Rich Phases on Oxide Films in Al-11.5Si-0.4Mg Cast Alloys, *Metall. Mater. Trans. A*, 2003, **34A**, p 1409–1420
5. R. Raiszadeh and W.D. Griffiths, A Semi-Empirical Mathematical Model to Estimate the Duration of the Atmosphere within a Double Oxide Film Defect in Pure Aluminium Alloy, *Metall. Mater. Trans. B*, 2008, **39B**, p 298–303
6. R. Raiszadeh and W.D. Griffiths, The Behaviour of Double Oxide Film Defects in Liquid Al Alloys Under Atmosphere and Reduced Pressures, *J. Alloys Compd.*, 2009, **491**, p 575–580
7. W.D. Griffiths and N.W. Lai, Double Oxide Film Defects in Cast Magnesium Alloy, *Metall. Mater. Trans. A*, 2007, **38**(1), p 190–196
8. J. Campbell, *Castings Practice, the 10 Rules of Castings*, 1st ed., Elsevier Butterworth-Heinemann, Oxford, 2004
9. T. Din, R. Kendrick, and J. Campbell, Direct Filtration of A356 Al Alloy, *AFS Trans.*, 2003, **017**, p 91–100
10. D. Dispinar and J. Campbell, Metal Quality in Secondary Remelting of Aluminium, *Foundry Trade J.*, 2004, **178**(3612), p 78–81
11. A. Habibollahzadeh and J. Campbell, Metal Flow Through a Filter System, *AFS Trans.*, 2002, **020**, p 19–35
12. H. Hashemi and R. Raiszadeh, Naturally-Pressurized Running System: The Role of Ceramic Filters, *J. Appl. Sci.*, 2009, **9**(11), p 2115–2122
13. Y. Yang, H. Nomura, and M. Takita, Inclusion Removal Using Ceramic Foam Filters and Filter Size Estimation, *Int. J. Cast Met. Res.*, 1996, **9**, p 27–35
14. L.J. Gauckler, M.M. Waeber, C. Conti, and M. Jacob-Daliere, Ceramic Foam for Molten Metal Filtration, *J. Met.*, 1985, **37**, p 47–50
15. B. Vernescu, D. Apelian, and J.L. Hoffmann, Deep Bed Filtration for Molten Metals, *International Conference on Porous Media and their Applications in Science, Engineering and Industry*, Kailua-Kona, Hawaii, 1996, p 1–9
16. A. Ciftja, T.A. Engh, and M. Tangstad, A Model of Foam Filters, *Metall. Mater. Trans. B*, 2010, **41B**, p 146–150
17. T.A. Engh, *Removal of Inclusions*, Oxford University Press, New York, 1992
18. C. Tien and B.V. Ramarao, *Granular Filtration of Aerosols and Hydrosols*, 2nd ed., Elsevier, Amsterdam, 2007

19. N.R. Green and J. Campbell, Statistical Distributions of Fracture Strengths of Cast Al-7Si-Mg Alloy, *Mater. Sci. Eng. A*, 1993, **173**, p 261–266
20. D.R. Poirier and G.H. Geiger, *Transport Phenomena in Materials Processing*, 2nd ed., The Minerals, Metals & Materials Society, Warrendale, PA, 1994
21. R. Raiszadeh, *A Method to Study the Behaviour of Double Oxide Film Defects in Aluminium Alloys*, Metallurgy and Materials Department, The University of Birmingham, Birmingham, UK, 2006, p 267
22. E.A. Brandes and G.B. Brook, *Smithells Metals Reference Book*, 7th ed., Butterworth-Heinemann, Oxford, 1999
23. H.I. Joo, K. Duncan, and G. Ciccarelli, Flame-Quenching Performance of Ceramic Foam, *Combust. Sci. Technol.*, 2006, **178**(10-11), p 1755–1769
24. N.J. Keegan, W. Schneider, and H.P. Krug, Evaluation of the Efficiency of Fine Pore Ceramic Foam Filters, Light Metals (TMS), 1997, p 973–982
25. S. Ray, B. Milligan, and N. Keegan, Measurement of Filtration Performance, Filtration Theory and Practical Applications of Ceramic Foam Filters, *9th Australian Conference and Exhibition on Aluminum Cast House Technology*, 2005, p 1–12
26. M. Gauthier, L.P. Lefebvre, Y. Thomas, and M.N. Bureau, Production of Metallic Foams Having Open Porosity Using a Powder Metallurgy Approach, *Mater. Manuf. Process.*, 2004, **19**(5), p 793–811